Normal-reflection image

Lianjie Huang and Michael C. Fehler, Los Alamos National Laboratory*

Summary

Common-angle wave-equation migration using the double-square-root is generally less accurate than the common-shot migration because the wavefield continuation equation for the former involves additional approximations compared to that for the latter. We present a common-angle wave-equation migration that has the same accuracy as common-shot wave-equation migration. An image obtained from common-angle migration is a four- to five-dimensional output volume for 3D cases. We propose a normal-reflection imaging condition for common-angle migration to produce a 3D output volume for 3D migration. The image is closely related to the normal-reflection coefficients at interfaces. This imaging condition will allow amplitude-preserving migration to generate an image with clear physical meaning.

Introduction

As exploration for new natural resources takes place in complex regions that are increasingly difficult to image and increasingly expensive to drill, there are more challenging demands placed on our ability to accurately characterize complex regions for reliable resource assessment. These demands are particularly pronounced for regions like deepwater or those containing sub-salt structures in the United States Gulf of Mexico. Images obtained from the angle domain provide more information about reflector physical properties than conventional migration images. This has led to a great interest in common-angle wave-equation migration, because compared to Kirchhoff migration, wave-equation migration has the potential to produce more-accurate and better-quality images of complex structures (Fehler and Huang, 2002).

Most current common-angle wave-equation migration is based on the double-square-root operator (Mosher and Foster, 2000; Kuehl and Sacchi, 2001; Jin et al., 2002). They often need to make additional approximations in the wavefield downward continuation equation for common-shot migration (e.g. Jin et al., 2002). This makes the common-angle migration less accurate than common-shot migration.

In this paper, we present a common-angle wave-equation migration method that uses common-shot gathers and maintains the accuracy of the wavefield downward continuation equation. A common-angle migration image is a four- to five-dimensional output volume for 3D cases (Xie and Wu, 2002). The size of such 4D to 5D images for large three-dimensional imaging problems is huge, and it is very difficult to analyze those images due to high dimensionality and large data volume.

The reflection coefficient at an interface is a function of incidence/reflection angle as well as the contrast in properties across the interface. The conventional imaging condition simply combines images for all different incidence/reflection angles, and the corresponding image is not well related to physics. Because the physical meaning of such an image is not clear, the interpretation of migration results cannot be well founded in terms of physics.

In this paper, we propose a new migration imaging condition that combines common-angle images for different incidence/reflection angles using an angle-dependent weight. Therefore, the output volume of this imaging condition will be three dimensional for 3D cases, rather than four- to five-dimensional. The new image is the normal-reflection image that is proportional to the normal-reflection coefficients at interfaces for amplitude-preserving migration.

Common-angle wave-equation migration

We present in the following a common-angle wave-equation migration scheme using common-shot gathers. The migration image $I(x,z)$ for common-shot wave-equation migration for 2D cases is given by

$$I(x,z) = -\sum_{\omega} i\,\omega \frac{U_r(x,z;\omega)}{U_s(x,z;\omega)}, \qquad (1)$$

or by

$$I(x,z) = -\sum_{\omega} i\,\omega\, U_r(x,z;\omega)\, U_s^{\star}(x,z;\omega), \qquad (2)$$

where $i=\sqrt{-1}$, (x,z) is the space position, ω is the circular frequency, U_r is the downward-continued recorded-wavefield obtained using a wave-equation migration propagator, U_s is the incident wavefield from a source, and "$\star$" represents the complex conjugate.

The horizontal component of ray parameter for reflections can be written in terms of the wavenumber and the circular frequency as

$$P_x^r = \frac{k_x}{\omega} = \frac{\sin\theta_r}{v(x,z)}, \qquad (3)$$

where k_x is the horizontal component of wavenumber, θ_r is the angle between the reflection and vertical directions (see Figure 1), and $v(x,z)$ is the velocity at position (x,z).

For common-angle migration, we obtain an image for a given value of P_x^r by selecting one value of k_x for each ω. Therefore, U_r in equation (1) or (2) is obtained from

$$U_r(x,z;\omega) = \mathcal{F}^{-1}\left\{U_r(k_x,z;\omega)\, F(k_x)\right\}, \qquad (4)$$

where $\mathcal{F}^{-1}$ denotes the inverse Fourier transform over k_x, and $F(k_x)$ is a narrow-bandpass filtering function such as a Butterworth filter (see Figure 2a), which is 1.0 at a given value of k_x and is very small at k_x other than the given value.

For a given ray parameter P_x^r and a given circular frequency ω, the corresponding wavenumber k_{x_j} may not be at a discrete

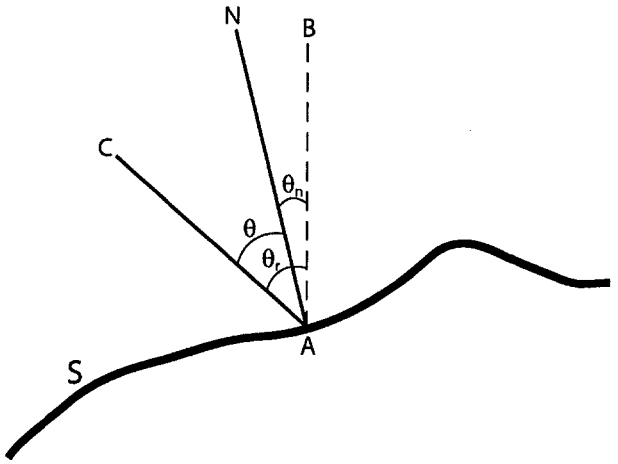

FIG. 1. Illustration of the angle between reflection and vertical direction (θ_r), the angle between the normal and vertical directions (θ_n), and the reflection angle θ at a location "A" on an interface "S".

point of k_x, but lies between the discrete points k_{x_i} and $k_{x_{i+1}}$ (see Figure 2b). For such cases, we use the wavefields at k_{x_i} and $k_{x_{i+1}}$ to linearly interpolate the wavefield at k_{x_j}.

In the same way as above, one can also obtain common-angle images for different values of ray parameter P_x^s for incident wavefields. This will produce five-dimensional output image volume for 3D cases (Xie and Wu, 2002)

The common-angle wave-equation migration propagator in the common-shot domain has the same accuracy as the common-shot wave-equation migration propagator, and is more accurate than the corresponding common-angle wave-equation migration in the offset domain that involves additional approximations in the propagator for common-shot migration.

Normal-reflection imaging condition

The conventional migration imaging condition (1) or (2) gives an image that combines different incidence and reflection angles, and therefore, the physical meaning of the image is not clear.

Common-angle migration images can provide images as a function of incidence/reflection angles, but the image volumes are three to four dimensions for 2D cases, and four to five dimensions for 3D cases. The sizes of the image volumes are significantly larger than conventional images obtained using equation (1) or (2). In addition, it would very difficult to visualize an image that is larger than three dimensions.

In the AVO (amplitude-versus-offset) studies, the reflection coefficient R at an interface is expanded in terms of the reflection angle θ and approximated (Shuey, 1985; Simmons, Jr. and Backus, 1994). For scalar waves in constant-density media, such an approximation can be simplified as (e.g. Červený and Lloyd, 2001)

$$R(x,z;\theta) \approx \frac{R_n(x,z)}{\cos^2\theta}, \tag{5}$$

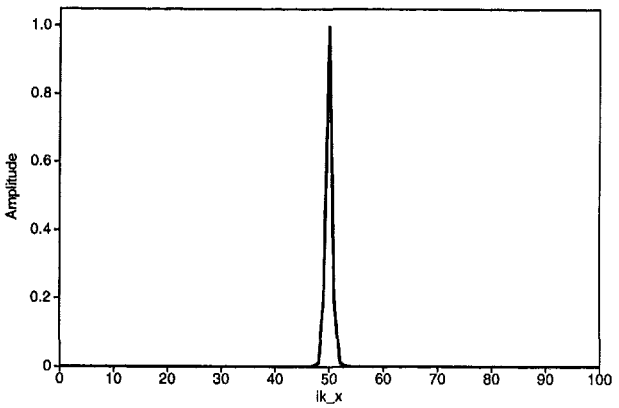

(a) Narrow-bandpass Butterworth filter

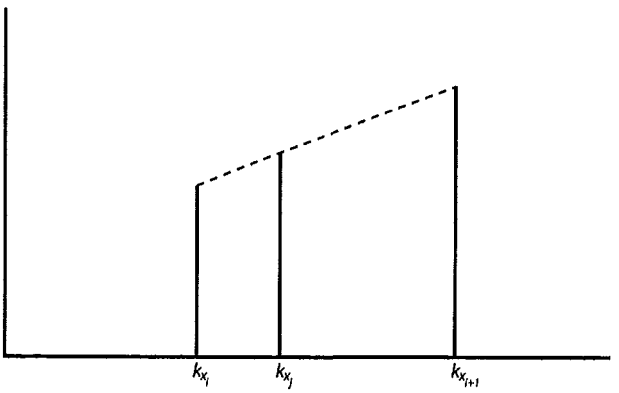

(b) Linear interpolation

FIG. 2. (a) A very narrow-bandpass Butterworth filter used as F in equation (4). (b) The wavefield at k_{x_j} is obtained by linearly interpolating those at k_{x_i} and k_{x_j}.

where R_n is the reflection coefficient for normal incidence, and the reflection angle $\theta = \theta(x,z)$ is given by (see Figure 1)

$$|\theta(x,z)| = |\theta_r(x,z) - \theta_n(x,z)|, \tag{6}$$

where θ_n can be calculated from a smoothed slowness model, and θ_r can be obtained using equation (3),

$$\theta_r(x,z) = \sin^{-1}\left[P_x^r\, v(x,z)\right]. \tag{7}$$

Equation (5) is accurate for small angles of reflection (Červený and Lloyd, 2001). The reflection angles at interfaces are usually small due to limited recording apertures in the real data acquisition, particularly for deep reflectors.

From equation (5), we have

$$R_n(x,z) \approx R(x,z;\theta)\, \cos^2\theta\,. \tag{8}$$

Therefore, we propose the following imaging condition:

$$I_n(x,z) = \sum_{\theta} I(x,z;\theta)\, \cos^2\theta, \tag{9}$$

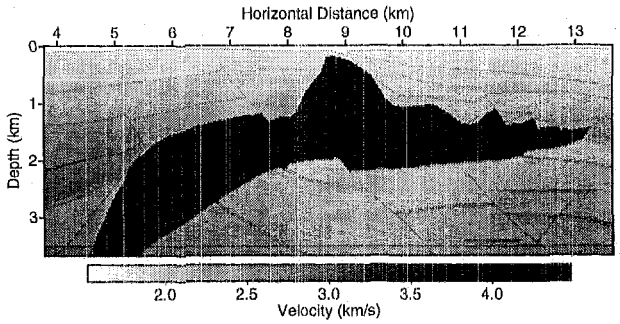

FIG. 3. A 2D slice of the SEG/EAGE salt model. The salt body is shown in black.

where $I(x, z; \theta)$ is the common-angle migration image. The image $I_n(x, z)$ obtained from equation (9) can be considered as an image that is proportional to the normal reflection coefficient at each interface position. Therefore, the image $I_n(x, z)$ is termed the normal-reflection image. This image has the same dimension as that of the image space.

Migration Examples

We used a common-shot dataset for a 2D slice of the SEG/EAGE salt model (Aminzadeh et al., 1996) shown in Figure 3 to produce normal-reflection images. The dataset was generated by O'Brien and Gray (1996) using a full-wave-equation finite-difference scheme. The synthetic dataset contains 325 common-shot gathers, and each shot-gather consists of 176 receivers with an interval of 24.384 m. The shot interval is twice the receiver spacing. The model was defined in a grid with the horizontal and vertical grid spacings of both 24.384 m. The frequency range used for migration was 2–30 Hz.

Figures 4(a)–(c) are normal-reflection images obtained using different ranges of reflection angle during common-angle migration. For comparison, a conventional migration image is shown in Figure 4(d). All migrations were conducted using the globally optimized Fourier finite-difference migration method (Huang and Fehler, 2000). Figures 4(a)–(c) contains fewer numerical artifacts within and beneath the salt body than Figure 4(d).

Figure 5 shows differences among normal-reflection images in Figures 4(a)–(c). The differences of images beneath the salt body shown in Figure 5(a) are small. This demonstrates that the incidence/reflection angles at interfaces in those regions are mostly less than 15°. The difference shown in Figure 5(b) is insignificant and therefore, the incidence/reflection angles at interfaces for the common-shot dataset for the salt model in Figure 3 are mostly less than 30°.

Ultimately, many other factors such as amplitude-preserving and limited-illumination effects must be taken into account to obtain a realistic normal-reflection image that is proportional to normal reflection coefficients.

Conclusions

We have proposed a common-angle wave-equation migration using common-shot gathers. It can generate more accurate

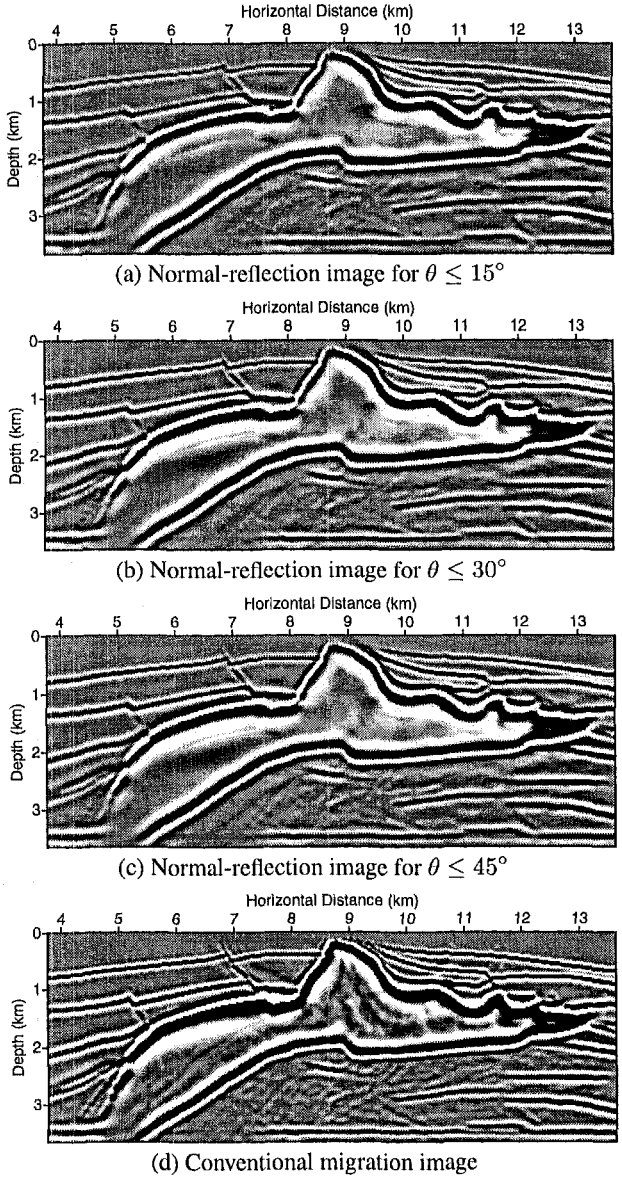

(a) Normal-reflection image for $\theta \leq 15°$

(b) Normal-reflection image for $\theta \leq 30°$

(c) Normal-reflection image for $\theta \leq 45°$

(d) Conventional migration image

FIG. 4. (a)–(c) are normal-reflection images for different ranges of reflection angle and (d) is a migration image obtained using imaging a conventional imaging condition (2).

common-angle images than methods based on the survey sinking (or the double-square-root) because the former does not involve any approximations used in the latter. However, the size of 4D to 5D images of common-angle migration for large three-dimensional imaging problems is huge, and it is very difficult to analyze such images due to their high dimensionality and huge data volume.

To reduce the data volume of common-angle migration images and obtain a migration image with a clear physical meaning, we have developed a new migration imaging condition to

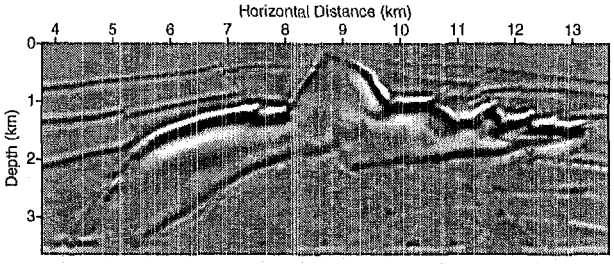

(a) Difference between images in Figures 4(a) and (b).

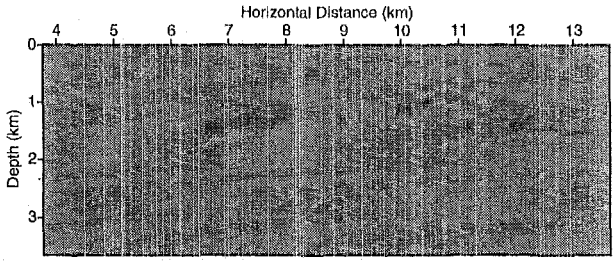

(b) Difference between images in Figures 4(b) and (c).

FIG. 5. Differences among the normal-reflection images in Figure 4.

produce a normal-reflection image. Such an image is proportional to the normal-reflection coefficients at interfaces. The normal-reflection imaging condition proposed in this paper can also be applied to the common-angle Kirchhoff migration (Xu et al., 2001).

Acknowledgments

This work was supported by the U.S. Department of Energy through contract W-7405-ENG-36 to Los Alamos National Laboratory. We thank John E. Anderson at ExxonMobil for his helpful discussions.

References

Aminzadeh, F., Burkhard, N., Long, J., Kunz, T., and Duclos, P., 1996, Three dimensional SEG/EAEG models — an update: The Leading Edge, **15**, No. 2, 131–134.

Červený, V., and Lloyd, M., 2001, Seismic Ray Theory: Cambridge Univ. Press, Cambridge.

Fehler, M., and Huang, L., 2002, Modern imaging using seismic reflection data: Ann. Rev. Earth. Planet. Sci., **30**, 259–284.

Huang, L., and Fehler, M. C., 2000, Globally optimized Fourier finite-difference migration method: 70th Ann. Internat. Mtg., Soc. Expl. Geophys., Expanded Abstracts, 802–805.

Jin, S., Mosher, C., and Wu, R.-S., 2002, Offset-domain pseudoscreen prestack depth migration: Geophysics, **67**, 1895–1902.

Kuehl, H., and Sacchi, M., 2001, Generalized least-squares dsr migration using a common angle imaging condition: 71st Ann. Internat. Mtg, Soc. of Expl. Geophys., Exapanded Abstracts, 1025–1028.

Mosher, C., and Foster, D., 2000, Common angle imaging conditions for prestack depth migration: 70th Ann. Internat. Mtg, Soc. of Expl. Geophys., Expanded Abstracts, 830–833.

O'Brien, M. J., and Gray, A. H., 1996, Can we image beneath salt?: The Leading Edge, **15**, No. 1, 17–22.

Shuey, R. T., 1985, A simplification of the zoeppritz equations: Geophysics, **50**, 609–614.

Simmons, Jr., J. L., and Backus, M. M., 1994, Avo modeling and the locally converted shear wave: Geophysics, **59**, 1237–1248.

Xie, X., and Wu, R., 2002, Extracting angle domain information from migrated wavefield: 72nd Ann. Internat. Mtg, Soc. of Expl. Geophys., Exapanded Abstracts, 1360–1363.

Xu, S., Chauris, H., Lambare, G., and Noble, M. S., 2001, Common-angle migration: A strategy for imaging complex media: Geophysics, **66**, 1877–1894.